Scientific Research Publishing

World Journal of Condensed Matter Physics, 2026, 16(4), 91-115
https://www.scirp.org/journal/wjcmp
ISSN Online: 2160-6927
ISSN Print: 2160-6919

Structural, Magnetic, and Microwave Absorption Properties of Al^{3+} Doped Low-Sintered $BaFe_{12}O_{19}$ Hexaferrite

Yaseen Mohd[1], Deepika Sharma[2*], Rohit Duglet[2], Vijay Singh[2], Sonia Khan[3], Mahavir Singh[2], Indu Sharma[2]

[1]Center for Green Energy Research, Department of Physics, CPU, Hamirpur, India
[2]Department of Physics, Himachal Pradesh University, Shimla, India
[3]Institute of Vocational (Tourism) Studies, Himachal Pradesh University, Shimla, India
Email: *deepika19399@gmail.com

How to cite this paper: Mohd, Y., Sharma, D., Duglet, R., Singh, V., Khan, S., Singh, M. and Sharma, I. (2026) Structural, Magnetic, and Microwave Absorption Properties of Al^{3+} Doped Low-Sintered $BaFe_{12}O_{19}$ Hexaferrite. *World Journal of Condensed Matter Physics*, **16**, 91-115.
https://doi.org/10.4236/wjcmp.2026.164006

Received: August 2, 2026
Accepted: September 20, 2026
Published: September 23, 2026

Abstract

Hexaferrite materials emerge as multifunctional materials with effective magnetic and microwave absorption properties, which contribute to modern electrical mobility and radar applications. In this work, we present a comprehensive analysis of the $BaFe_{12-x}Al_xO_{19}$ (x = 0.00, 0.02, 0.04, 0.06, and 0.08) series, synthesized via the citrate precursor route. Structural and Fourier transform infrared (FTIR) analysis established the M-type hexagonal phase for all studied compounds. Magnetic results reveal the hard ferromagnetic nature of the investigated compounds. In addition, crystallographic parameters, metal-oxygen stretching, bending vibrations, and magnetic characteristic parameters were also tuned with the doping concentration. Besides, microwave absorption behavior in terms of complex permittivity and permeability across different target bands is also examined. The result divulges the synergistic effects of dielectric/magnetic loss and strong electromagnetic attenuation, enabling efficient microwave absorption/reflection loss, a wide effective absorption bandwidth, and a thin matching thickness. The reported results demonstrate that tuning the nonmagnetic Al^{3+} doping in M-type hexaferrites provides an effective avenue to alter the magnetic and microwave absorption properties, suggesting its potential in communication technology.

Keywords

M-Type Ferrite, Magnetic Properties, Permanent Magnet, EM Properties, mW Absorption

1. Introduction

With a significant influence on the globe's GDP, employment, and international trade, tourism has become the most significant economic industry in the world. Serious concerns about resource depletion, environmental sustainability, and the effects of climate change have been raised by this massive increase. This makes it crucial to understand how tourism development may align with green growth objectives [1]-[3]. Using inexpensive, readily available, non-toxic, and environmentally acceptable magnetic material is one method to integrate tourism with green energy aims. The usage of expensive, rare-earth permanent magnets (PM) in electric vehicles (EVs) and electromagnetic (EM) interference in telecommunication applications are the two main environmental issues that are concurrently addressed in this original article [4] [5]. The motors in EVs are crucial to their functioning. Scientists have been searching for an EV motor substitute that doesn't contain rare earth elements for the past few years [6]. However, because of the widespread usage of wireless devices and communication devices that operate at different frequencies, microwave (mW) absorbers are needed to prevent electromagnetic interference [5]. Ferrite NPs appear to be the most promising multifunctional material to actively address both issues at the same time because of their special combination of dielectric and magnetic properties [7]. Ferrite's exceptional magnetic behaviour has garnered a lot of interest [8]. These materials are useful in magnetic energy conversion, data storage, spintronics, mW devices, PM in EVs, and electromagnetic interference (EMI) shielding due to their low cost, good stability, high electrical resistivity, and magnetic properties (high coercivity and large crystalline anisotropy) [9]-[11]. To actively address this challenge, ferrite NPs come out as the likely-looking multi-functional material because of their outstanding combination of magnetic and dielectric properties [7]. Ferrites have attracted significant attention due to their excellent magnetic behavior [12]. Along with their low cost, good stability, high electrical resistivity, and magnetic properties (high coercivity and large crystalline anisotropy), these materials are beneficial in magnetic energy conversion, data storage, spintronics, mW devices, and electromagnetic interference (EMI) shielding [13]-[16]. Based on magnetic properties and crystal structure, ferrites can be classified into distinct forms. From the viewpoint of crystal structure, ferrites are divided into four types: spinel, garnet, ortho, and hexagonal. In addition, based on their magnetic properties, ferrites can be categorized in two ways: named as soft ferrite and hard ferrite, or hexaferrite (HF) [16].

According to their chemical makeup and molecular arrangement (of S, R, and T blocks) in the hexagonal crystal lattice, the HF are divided into six main varieties, as illustrated in **Table 1** [17].

It is observed here that X is Ba^{2+}, Sr^{2+} and Pb^{2+} or the fusion of these ions in different proportions. Me is a transition metal ion, such as Co^{2+}, Fe^{2+}, Ni^{2+}, Mn^{2+}, Zn^{2+}, Zr^{4+}, or a mix of these ions. A 180-degree rotation of the matching subunit around the hexagonal axis is indicated by the asterisk (*). Hexagonal BHF is

Table 1. Different types of Hexaferrite material based on chemical composition.

Hexaferrite	Chemical composition	HF slabs	Number of unit cells
M	$XFe_{12}O_{19}$	S R S* R*	2M
W	$XMe_2Fe_{16}O_{27}$	S S R S* S* R*	2W
X	$A_2Me_2Fe_{28}O_{46}$	3(S R S* S* R*)	3X
Y	$A_2Me_2Fe_{12}O_{22}$	3(S T)	3Y
Z	$A_3Me_2Fe_{24}O_{41}$	S T S R S* T* S* R*	2Z
U	$A_4Me_2Fe_{36}O_{60}$	S R S* R* S* T*	U

frequently utilized in mW devices and PM material in EV applications [18]. Because of their high magnetic saturation (M_s), coercivity (H_c), Curie temperature, chemical stability, and strong corrosion resistance, M-type HF materials are quite desirable over other ferrite materials [17]. **Table 2** below gives the comparative analysis of the work done by various researchers to see the mW absorption properties of M-type ferrite materials.

Table 2. The comparative analysis of mW absorption properties of the M-type ferrite material.

Name	Composition	x	RL_{min} (dB)	Thickness (nm)	Matching Frequency (GHz)	EAB (GHz)	Ref.
Kaur *et al.*	$Ba_{0.5}Sr_{0.5}Co_{0.4}In_{0.4}Fe_{12.2}O_{19}$	-	−32.15	1.6	12.4	10.38 - 12.4 (2.02)	[19]
		-	−27.67	1.7	11.64	9.71 - 12.4 (2.69)	
		-	−20.86	1.8	10.97	8.6 - 12.31 (3.71)	
Duglet *et al.*	$BaBi_xFe_{12-x}O_{19}$	0.00	−3.89	5.2	-	-	[15]
		0.05	−15.6	2.2	10.7	12.05 - 12.50 (0.45)	
		0.10	−38.78	2.8	12.2	11.46 - 12.47 (1.01)	
Liao *et al.*	$BaFe_{12-3X}(GdAlCo)_xO_{19}$	0.3	−48.13	2.07	11.75	9.73 - 15.27 (5.54)	[20]
		0.3	−31.33	2.0	12.1	9.9 - 15.88 (5.98)	
		0.4	−23.68	2.0	11.84	9.38 - 13.07 (3.69)	
		0.4	−42.69	2.5	9.38	7.71 - 12.1 (4.39)	
Naqvi *et al.*	$SrCo_xNi_xFe_{12-2x}O_{19}$	0.2	−22.22	9.8	9.46	9.38 - 9.8 (0.42)	[21]
		0.2	−22.35	9.9	9.54	9.38 - 9.8 (0.42)	
		0.2	−24.94	10.0	9.55	9.38 - 9.8 (0.42)	
		0.6	−23.03	9.9	9.63	8.96 - 9.8 (0.84)	
		0.6	−30.43	10.0	9.04	8.96 - 9.71 (0.75)	

The magnetic orientation of Fe^{3+} in M-type HF is responsible for its hard-magnetic characteristics. **Figure 1** shows the structure of the magneto-plumbite M-type HF. Five distinct crystal sites, such as 3 octahedral (2a, 12k, and 4f2), 1 tetrahedral (4f1), and 1 trigonal bipyramidal (2b) site, are home to Fe^{3+} ions in the M-type HF structure. In the magnetized oriented form of BHF, the spins of the 12k,

2a, and 2b sites are parallel to one another along the crystallographic c-axis, whereas the $4f_2$ and $4f_1$ sites point in the other direction [22]. By replacing these Fe^{3+} ions in the hexagonal lattice with different divalent and trivalent cations, these materials' microstructure and magnetic characteristics can be altered. Tuning the structural and other related functional properties in HF materials via their constituent elements can lead to distinct functionality and is important for both fundamental and technological viewpoints. In this regard, trivalent (Al^{3+}) doping in M-type $BaFe_{12}O_{19}$ could be a beneficial option to tailor their multifunctional properties and underlying physics.

Therefore, in this manuscript, we have systematically investigated the structural, morphological, magnetic and microwave absorption properties of the $BaFe_{12-x}Al_xO_{19}$ (x = 0.00, 0.02, 0.04, 0.06, and 0.08) series prepared by the citrate precursor method. Structural analysis confirms the M-type hexagonal phase in all investigated series of samples. The sample morphology and grain size distribution further support our findings. FTIR analysis also verified the hexagonal crystalline phase, as evidenced by metal-oxygen stretching and bending vibrations. Magnetic results demonstrate the hard ferromagnetic characteristics of BHF and further tailor the magnetic characteristics with doping concentration. Moreover, microwave absorption ability is also scrutinised in terms of complex permittivity and permeability in the different targeting bands. The result divulges the synergistic effects of dielectric/magnetic loss and strong electromagnetic attenuation, enabling efficient microwave absorption/reflection loss, a wide effective absorption bandwidth and a thin matching thickness. The results of trivalent nonmagnetic doping in BHF also affect the absorption parameters, along with other properties, suggesting its potential in communication technology.

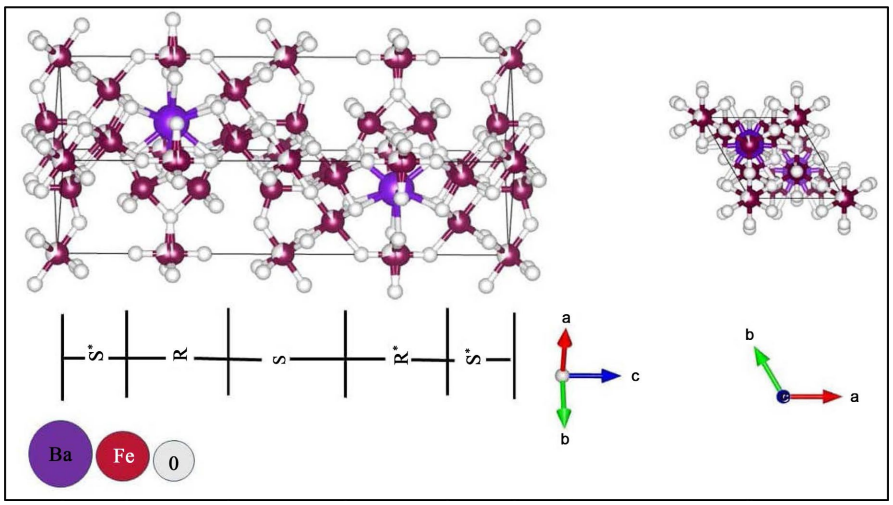

Figure 1. Magneto-Plumbite structure of M-type BHF.

2. Experimental Details

Researchers have used different types of methods, such as ball-milling [23] [24],

laser evaporation [25], co-precipitation [26] [27], sol-gel [28] [29], citrate precursor [30] and sol-gel auto combustion [31], etc., for the formation of ferrite magnetic nanoparticles (MNP). In this study, the citrate precursor method was used to create Al-doped M-type BHF nanoparticles (NP) having the chemical formula $BaFe_{12-x}Al_xO_{19,}$ where $x = 0.00$, 0.02, 0.04, 0.06, and 0.08. This technique maintains precise metal stoichiometry while allowing the creation of crystallites with well-defined grain sizes of approximately 50 nm [32]. In the chelate-based polymeric citrate precursor approach, mixed cations react with citric acid, and ethylene glycol is used to cross-link the cations during esterification. These inexpensive, sophisticated techniques produce consistent NPs with a narrow size distribution, are repeatable, and yield high-quality output for demand applications. Low-temperature synthesis techniques, such as polymeric citrate precursor, are effective enough to regulate the creation of unique NPs with distinct morphologies that result in innovative devices with the required technical capabilities [30]. **Figure 2** depicts the methodical process for M-type BHF formation. Barium nitrate ($Ba(NO_3)_{2)}$), Ferric nitrate ($Fe(NO_3)_3{\cdot}9H_2O$), Aluminium nitrate ($Al(NO_3)_3{\cdot}9H_2O$), and citric acid ($C_6H_8O_7$) were all precisely weighed in stoichiometric amounts as shown in **Table 3**. Citric acid and total metal nitrates were maintained at a 1:1 molar ratio. To create a homogeneous precursor solution, each precursor was dissolved independently in a small amount of deionized water. The ammonia solution was added dropwise to maintain a pH 7. The solutions were heated at a temperature of 80˚C. A soft, fine precursor powder was produced by gently evaporating the mixture until it was completely dry. The formed powder was calcinated at 700˚C, and then sintered at 850˚C for 5 hours.

Characterization Techniques:

The structural phase of matter was assessed using an X-ray diffractometer, Cu-Kα beam (λ = 0.15418 nm) in the 20 - 70 (2θ) range. An FTIR spectrometer (Bruker, Model - Tensor 27) was used to obtain transmission mode FTIR spectra to recognise the functional groups that exist and resonances of chemical bonds in

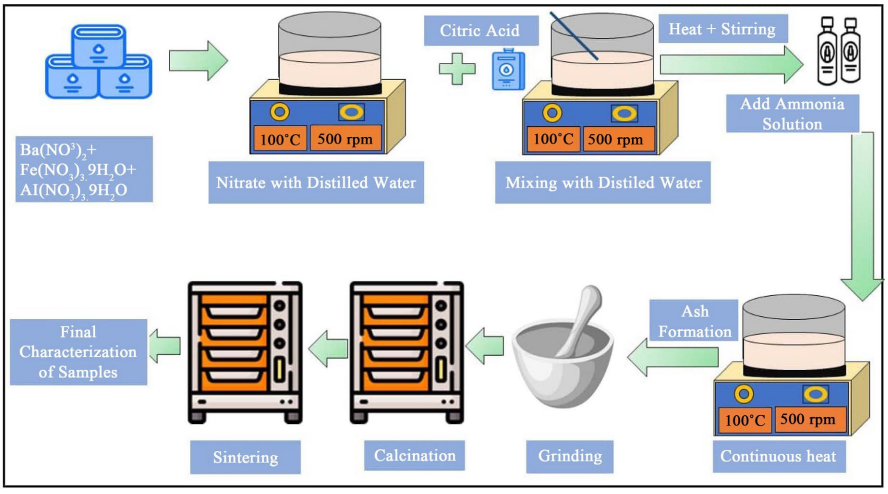

Figure 2. Citrate precursor method for the formation of Al-doped M-type BHF.

Table 3. The amount of nitrates (g), citric acid (g) and Ethylene Glycol (ml) used for the formation of Al doped M type BHF.

Formula used	Wt. of Barium Nitrate (g)	Wt. of Ferric Nitrate (g)	Wt. of Aluminium Nitrate (g)	Citric Acid (g)	Ethylene Glycol (ml)
$BaFe_{12}O_{19}$	1.87	34.87	0.00	17.94	2.23
$BaFe_{11.98}Al_{0.02}O_{19}$	1.88	34.84	0.054	17.96	2.23
$BaFe_{11.96}Al_{0.04}O_{19}$	1.88	34.78	0.108	17.96	2.24
$BaFe_{11.94}Al_{0.06}O_{19}$	1.88	34.73	0.162	17.96	2.24
$BaFe_{11.92}Al_{0.08}O_{19}$	1.88	34.72	0.216	17.99	2.44

ferrite nanoparticles. Using a JSM-IT800 Field Emission Scanning Electron Microscope (FE-SEM), the surface morphology of the samples was investigated. A vibrating sample magnetometer (VSM) (Lake Shore, Model 7404, range −10 kOe to +10 kOe) was used to measure magnetisation. The mW absorption properties were investigated in a varying frequency range of 1 - 12.00 GHz (L, S, C, and X-band) at room temperature (RT) using a Vector Network Analyser (VNA) (PNA, Agilent N5221B) connected to the DUT via coaxial cables. The VNA was calibrated before evaluating the scattering properties. For these measurements, the ferrite powder and polyvinyl alcohol (PVA) (also served as the polymer matrix) were mixed at a ratio of 95: 5 weight % of ferrite total composite mass. The mixture was compressed in a hydraulic press to form the toroidal ring which had an inner diameter of 3.04 mm, an outer diameter of 7.00 mm, and a pallet thickness of 2 - 3 mm. The coaxial transmission line holder was used to hold the toroidal samples. The Short- Open-Load-Through (SOLT) method was used to complete the two-port calibrations. The values of scattering parameters (S_{11} and S_{21}) were measured, and the Nicolson-Ross-Weir (NRW) technique was used to determine the complex permittivity and permeability.

3. Results and Discussion

3.1. X-Ray Diffraction Pattern

Figure 3 shows the XRD patterns of $BaFe_{12-x}Al_xO_{19}$ (where x = 0.00, 0.02, 0.04, 0.06, and 0.08 Nano-hexaferrites). According to the image, all samples' XRD pattern peaks matched space group P63/mmc and JCPD card No. 00 051-1879 [33]. The M-type HF peaks correspond to the hkl indexing of (110), (107), (114), (203), (205), (206), (217), (304), (220), and (219). These planes confirm the formation of the M-type hexagonal phase.

For M-type BHF with Al concentration (x) = 0.00 - 0.02, the M-type HF continues to be the predominant phase, but traces of the impurity phase start appearing with the increase in doping concentration. As the amount of dopant concentration increases from x = 0.04 - 0.08, the M-type phase remains as the predominant phase containing hematite [34]. As the dopant concentration increases, the intensity of the peaks of the hematite phase increases. This shows that the solubility of aluminium in the BHF phase is lower at 850˚C. This could be due to the

smaller ionic radii of Al^{3+} ions as compared to Fe^{3+} ions. The solubility of Al^{3+} ions in Fe^{3+} could be improved by increasing calcination temperature and time [35] [36].

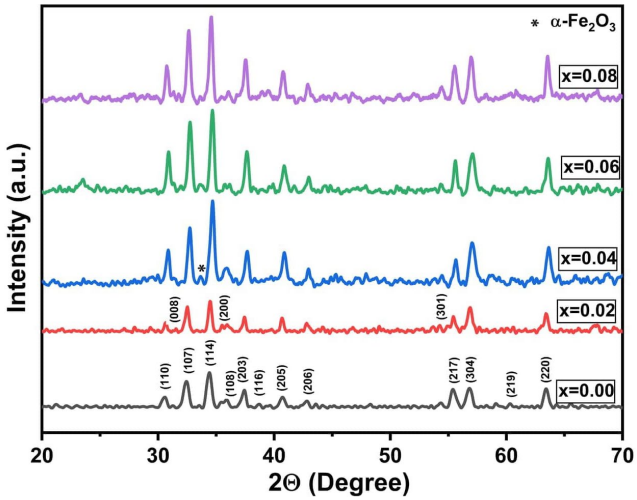

Figure 3. X-Ray Diffraction Pattern for $BaFe_{12-x}Al_xO_{19}$ where $x = 0.00$, 0.02, 0.04, 0.06, and 0.08.

The values of the lattice parameters are given in **Table 4**. **Figure 4** also shows the variation of structural parameters with dopant concentration. The formula below is used to compute the lattice constants [37]:

Table 4. Variation of lattice parameters, cell volume, crystallite size, strain, dislocation density, and density of Pure and Al-doped BHF.

Atom	a (Å)	c (Å)	c/a	V_{cell} (Å^3)	Size (nm)	Lattice Strain (η)	Dislocation Density (1/nm^2)	Density ($\delta_{x\text{-ray}}$) g/cm^3
$x = 0.00$	5.863	22.554	3.846	671.40	18.128	0.11022	0.0031	5.49
$x = 0.02$	5.859	22.464	3.834	667.78	25.347	0.08107	0.00172	5.52
$x = 0.04$	5.839	22.045	3.775	650.92	22.326	0.09166	0.00219	5.66
$x = 0.06$	5.838	21.995	3.766	649.81	22.337	0.09057	0.00212	5.67
$x = 0.08$	5.846	22.268	3.809	659.00	23.817	0.08374	0.00179	5.58

$$\frac{1}{d_{hkl}^2} = \frac{4}{3}\left(\frac{h^2 + hk + k^2}{a^2}\right) + \frac{l^2}{c^2} \quad (1)$$

where d_{hkl} is the interplanar spacing and h, k. l are the Miller indices of the planes. For the undoped sample, the values of "a" and "c" are 5.863 Å and 22.554 Å, respectively. The value of the lattice parameters decreases as the dopant concentration increases from $x = 0.02$ to $x = 0.06$, and then increases for $x = 0.08$. Identical patterns are also seen in the cell volume, which ranges from 649.61 Å^3 to 671.40 Å^3. This shift is explained by the fact that the ionic radius of Al^{3+} (0.535 Å) is less

than that of Fe^{3+} (0.645 Å) [38].

Grain size determination D (hkl) was done using Scherrer's formula [39].

$$D = \frac{0.9\lambda}{\beta \cos\theta} \tag{2}$$

where the average crystallite size is denoted by D, the X-ray wavelength by λ, the full width at half maximum (FWHM) by β, and Bragg's angle by θ. The value of crystallite size varies from 18.128 nm to 25.34 nm for pure and Al-doped BHF. The graphical variation of crystallite size with dopant concentration is shown in Figure 4. Table 4 shows the c/a ratio of pure and Al-doped BHF, which falls between 3.766 and 3.846. In comparison to the sample including an Al dopant, the c/a ratio for pure BHF is closer to 3.98. The limit of c/a = 3.98 for the M-type HF indicates that the samples have formed a distinct M-type phase [40].

The crystallinity of the material is determined by using its dislocation density. The value of dislocation density decreases as the crystallinity increases and vice versa [41]. Equation (3) is used to compute its value, which is given by:

$$\delta = \frac{1}{D^2} \tag{3}$$

where D is the crystallite size calculated using the Scherrer formula. Their values are shown in Table 4 lies in the range of 0.00172 - 0.0031.

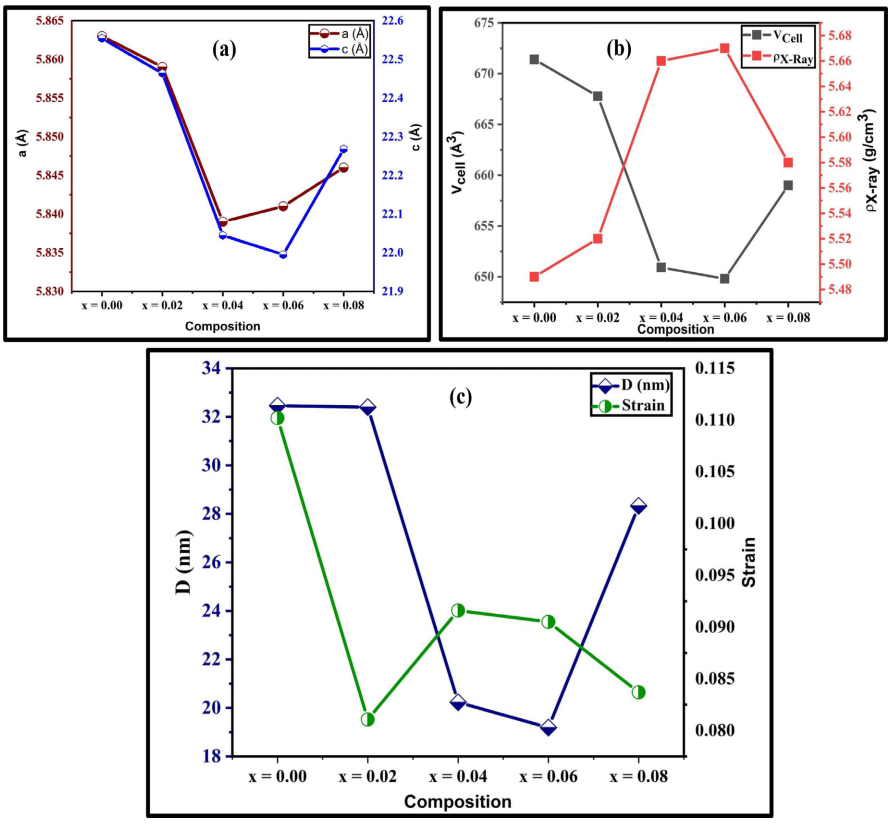

Figure 4. Variation of (a): Lattice parameters (b) Cell volume and X-ray density (c) Crystallite size and Starin with Al-doping concentration x = 0.00 - 0.08.

The formula [42] was used to determine the lattice strain (η) caused by doping.

$$\eta = \frac{\beta \cos\theta}{4} \tag{4}$$

The value of η lies in the range of 0.00107 to 0.11022. Its value is maximum for the undoped sample. Figure 4 shows the variation of η with dopant concentration. Analyzing the variation in the structural parameters is necessary to see the changes in magnetic and electromagnetic properties of the material.

3.2. SEM Analysis

FE-SEM micrographs of Al-doped BHF ($BaFe_{12-x}Al_xO_{19}$) are shown in Figure 5. Figures 5(a)-(c) corresponds to the micrographs and the lognormal distribution curve for $x = 0.02$, and Figures 5(d)-(f) for $x = 0.08$, respectively. The micrographs show the non-uniformity of the particle, where the micrographs predominantly display irregular, agglomerated particles.

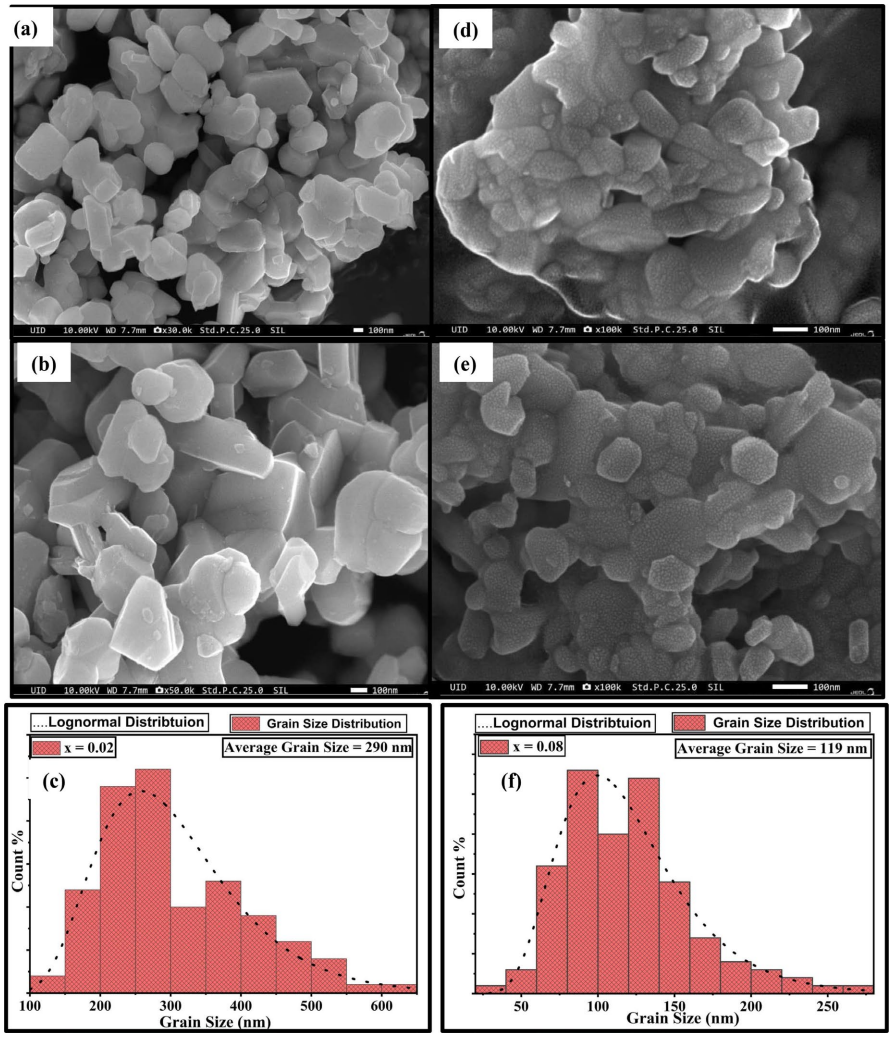

Figure 5. FE-SEM graphs and average grain size distribution graph for $BaFe_{12-x}Al_xO_{19}$ (a)-(c) For $x = 0.02$ (d)-(f) For $x = 0.08$ respectively.

The SEM clearly shows the visible spaces by means of porosity between the grains, which hinder the passage of charge at the grain boundaries. This will affect the polarisation and alter electrical properties, like the manner in which porosity affects magnetic properties [43]. The grain size distribution was examined using ImageJ software. **Figure 2(c)**, **Figure 2(f)** displays the distribution of grain size and histogram for composition $x = 0.02$ and $x = 0.08$. The average grain size is 290 nm at $x = 0.02$ and drops to 119 nm at $x = 0.08$. This decrease in grain size with increasing dopant concentration correlates well with the XRD-calculated variation in crystallite size.

3.3. FTIR Analysis

The infrared spectra of aluminium-substituted $BaAl_xFe_{12-x}O_{19}$ with x = 0.00, 0.02, 0.04, 0.06, and 0.08 are obtained in the 2500 - 400 cm^{-1} region. The absorption bands in the 1000 - 400 cm^{-1} region suggest that ferrites or inorganic ions are forming in the crystal lattice [44].

Atoms in HF are arranged in three distinct locations: tetrahedral, octahedral, and trigonal bipyramidal. **Figure 6** shows that for Al-doped BHF, the absorption bands are observed at 416 cm^{-1}, 568 cm^{-1}, 781 cm^{-1}, 1197 cm^{-1}, 1394 cm^{-1}, 1536 cm^{-1}, 1623 cm^{-1}, and 1702 cm^{-1}. A band centred around 418 cm^{-1} represents the stretching vibrations of Fe^{3+}-O^{2-} bonds at the octahedral sites inside the M-type HF. These are evidence of metal-oxygen and residual surface/precursor vibrations [45]. Two distinct absorption peaks between 540 - 580 cm^{-1} in the spectra indicate the stretching vibrations associated with Fe^{3+}-O^{2-} bonds confined at the tetrahedral locations [45]. The stretching vibrations of N-O are represented by the vibrational bands at 780 cm^{-1} [46]. The bands in the range of 1050 - 1150 cm^{-1} and 1350 - 1580 cm^{-1} are caused by the C-O stretching vibration and the bending vibration of C-H, respectively. The bands in the ranges of 1620 - 1680 cm^{-1} and 1700 - 1870 cm^{-1}, respectively, are caused by the stretching vibration of C=C and C=O [47].

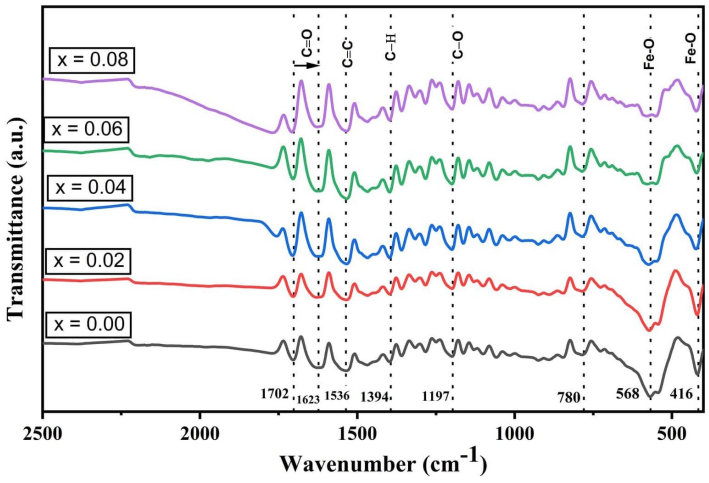

Figure 6. FTIR Spectra for pure and Al-doped M-type BHF ($BaFe_{12-x}Al_xO_{19}$ for $x = 0.00$ - 0.08).

3.4. Magnetic Study

Using the VSM, the magnetic characteristics of pure and Al-doped BHF ($BaFe_{12-x}Al_xO_{19}$, where $x = 0.00, 0.02, 0.04, 0.06$, and 0.08) powdered material were investigated at RT (300 K) under an applied magnetic field of 10 kOe. Figure 7 shows the hysteresis loop obtained from the pure and Al-doped BHF samples. The usual behavior of all magnetic isotherms and the presence of a strong, observable hysteresis loop confirm the hard ferromagnetic behavior with a large H_c, which is also consistent with the previously reported hard ferromagnetic nature of HF [14] [48]. Table 5 presents the obtained values of (magnetization at 10 kOe) M_s, M_r, and H_c for Al-doped BHF with different dopant concentrations, and Figure 8 illustrates their graphical change. Figure 8 shows that the magnetic property of doped BHF is significantly impacted by the Al^{3+} substitution. For pure BHF, the values of M_s, M_r, and H_c are 38.41 emu/g, 26.17 emu/g, and 3.04 kOe, respectively. With an increase in dopant concentration, the value of M_s and M_r. decreases from 34.41 emu/g and 22.83 emu/g for $x = 0.02$ to 25.73 emu/g, and 15.49 emu/g for $x = 0.08$.

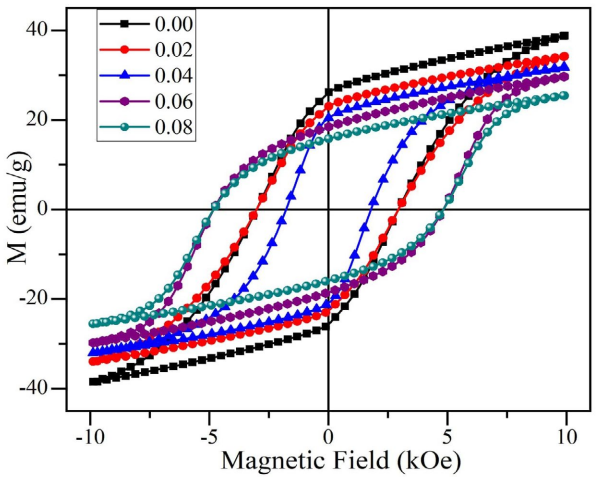

Figure 7. M-H curve of $BaFe_{12-x}Al_xO_{19}$, where $x = 0.00, 0.02, 0.04, 0.06$ and 0.08 respectively.

Table 5. variation of M_R (emu/g), M_S (emu/g), H_c (kOe), and M_R/M_s of $BaFe_{12-x}Al_xO_{19}$, where $x = 0.00, 0.02, 0.04, 0.06$, and 0.08.

Composition (x)	Remnant magnetization (emu/g)	Maximum magnetization (emu/g)	Coercive Field (kOe)	M_R/M_S
0.00	26.17	38.41	3.04	0.68
0.02	22.83	34.41	2.95	0.66
0.04	20.60	31.74	1.79	0.64
0.06	18.39	29.28	4.78	0.62
0.08	15.49	25.73	4.84	0.60

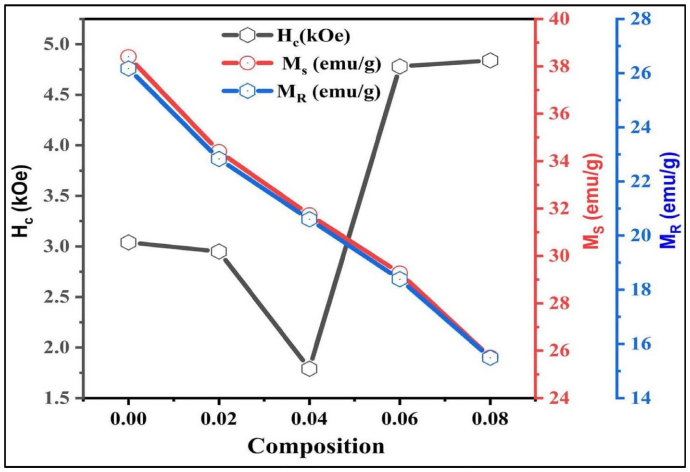

Figure 8. Variation of coercivity, saturation magnetization, and remanence with varying Al dopant concentration.

This magnetic attribute can be explained by the substitution of doped cations at different sites in the hexagonal structure of the ferrite. The magnetic moment in M-type HF is caused by the allocation of iron in five non-equivalent sublattices: 1 tetrahedral ($4f_1$), 1 trigonal bipyramidal (2b), and 3 octahedral (2a, 12k, and $4f_2$) [14]. Of these 5 locations, the electron spins at 12k (6), 2a (1), and 2b (1) are $\uparrow$, while those at $4f_1$ (2) and $4f_2$ (2) are $\downarrow$. Uncompensated upward spins are the cause of the total magnetic moment, or 20 μ_B. According to the literature, Al^{3+} primarily replaces Fe^{3+} in the 2a and 12k octahedral sites, with a lower but considerable fraction entering the $4f_2$ (octahedral) site, according to site occupancy refinements. The $4f_1$ (tetrahedral) site has just a small percentage (<5%), whereas the 4e (trigonal bipyramidal) site has a greater substitution for $x > 2$ [49]. The reduction in M_s and M_r of the synthesised materials is caused by the nonmagnetic Al^{3+} replacing the Fe^{3+} ion (having magnetic moment = 5 μ_B) from the sites with spin upward orientation, primarily 12k [38]. The super-exchange interaction between Fe^{3+}-O-Fe^{3+} also decreases when the diamagnetic Al^{3+} is substituted for Fe^{3+} ions [50] [51]. From this decrease in exchange contact, a non-collinear spin arrangement is formed. This decrease in exchange contact also initiates the randomly oriented arrangement of spins with respect to the c-axis in the surface layer [38]. Now, the coupling of canted surface spins with the c-axis-aligned core spin can further diminish the net magnetisation of the material.

The coercivity, H_c, first decreases from 3.04 kOe for $x = 0.00$ to 1.79 kOe for $x = 0.04$ before sharply increasing to 4.84 kOe for $x = 0.08$. The behaviour is somewhat similar to the previous reported results on Al dope M-type ferrite [38]. The maximum increment of 59.21% is observed with just 0.66% substitution of Fe^{3+} with Al^{3+} ions. The size of the particle and magneto-crystalline anisotropy are the two possible reasons for the observed influence of H_c on Al doping. The BHF NPs used in this investigation have a mean particle size between 100 nm and 300 nm. Luo *et al.* claim that as the amount of Al doping grows, the NPs' boundary of single domain (SD) increases and the grain size decreases [38]. The grains would

thus exhibit SD behaviour. The creation of an SD impeded the domain-wall movement, which results in the rise of H_c. However, domain wall role in defining H_c is difficult since defects can pin and nucleate domain barriers [38]. Additionally, when Al^{3+} is added as a replacement for Fe^{3+}, the H_c rises as predicted from $H_c = \alpha(2K/M_S)$ [52], where K is the magneto-crystalline anisotropy, and M_s is the magnetic saturation. This formula indicates that the H_c of the material increases as saturation magnetization decreases. This improvement in H_c behaviour is achieved with less than 0.7% Al substitution, demonstrating the effectiveness of aluminium doping in improving the hard magnetic properties of the material. This suggests that Al can serve as an efficient substitute to enhance coercivity, thereby optimizing magnetic performance for permanent magnet applications. Such a doping strategy offers a potential pathway towards developing a cost-effective, optimized ferrite-based material for high-performance applications, particularly in permanent magnetic technologies for electric vehicles.

3.5. EM Analysis and Loss Mechanisms

a) Permittivity and permeability

In complex permittivity, the real part (ε') is the indicator of electric energy storage and the imaginary part (ε'') of electric loss. Both parts are frequency-dependent. **Figure 9(a)**, **Figure 9(b)** represents the frequency-response of ε' and ε'' for the prepared samples. Up to ~8 GHz, except $x = 0.06$, all samples exhibit almost constant ε', indicating no space-charge and dipole polarisation lags. After 8 GHz ε' increase with frequency, this is more pronounced for the $x = 0.06$ sample observed after 6 GHz. This increase in ε' values with frequency may be attributed to resonance-type polarization dispersion instead of standard relaxation. Similar behaviour has been reported in the literature. G. Gultom *et al.* observed from 9.5 GHz to 10.5 GHz for Mg-Al doped and undoped barium FIG [53].

ε' is higher for the doped samples (the highest for $x = 0.04$) than undoped BHF. For ε'' variation with frequency, all the samples show wavy curves that arise from the effects of polarisation, especially interfacial and dipole polarisation. The Debye model is utilised to investigate polarisation effects (discussed in the Cole-Cole section). Almost all the samples followed a similar ε'' variation pattern as that of ε'. A discrepancy is seen for sample $x = 0.06$ after 8.5 GHz. Elevated values of ε'' are related to greater Ohmic losses and AC conductivity (dielectric relaxation). The relation of ε'' with electrical conductivity (σ) is well established (see Equation (5)) [54].

$$\sigma = 2\pi f \varepsilon_0 \varepsilon'' \tag{5}$$

where f is the varying frequency range, ε_0 stands for the permittivity of the free space, and ε'' is t imaginary value of complex permeability. Greater absorption requires a high value of ε'' to get a better attenuation constant value [15]. The quantity and kind of ions present in the material show the relaxation behaviour and determine the dielectric loss of ferrite. The presence of ferric (Fe^{3+}) and ferrous (Fe^{2+}) in the ferrite also affects the ε' and ε'', due to enhanced conduction

and electron hopping mechanisms [55]. **Figure 9(c)**, **Figure 9(d)** shows the frequency-dependent real and imaginary parts of complex permeability (μ' and μ''). The range of values for the real part of permeability over a broad frequency range of 1 - 12 GHz for pure BHF is (1.21 - 1.33). At $x = 0.00$, the value of μ' is 1.33 at 1 GHz. The greatest value of 1.4 for μ' is found at 1 GHz for composition $x = 0.04$. On the other hand, the value of μ'' remains close to zero over the frequency range of 1 - 12 GHz. The resonance peaks are also observed for the magnetic samples. The lowest value of imaginary permeability is observed for the composition of $x = 0.06$. G. Wang claims that hysteresis loss, ferromagnetic resonance loss, eddy current (EC) loss, and intergranular domain wall loss are the causes of magnetic energy dissipation in ferrite [56].

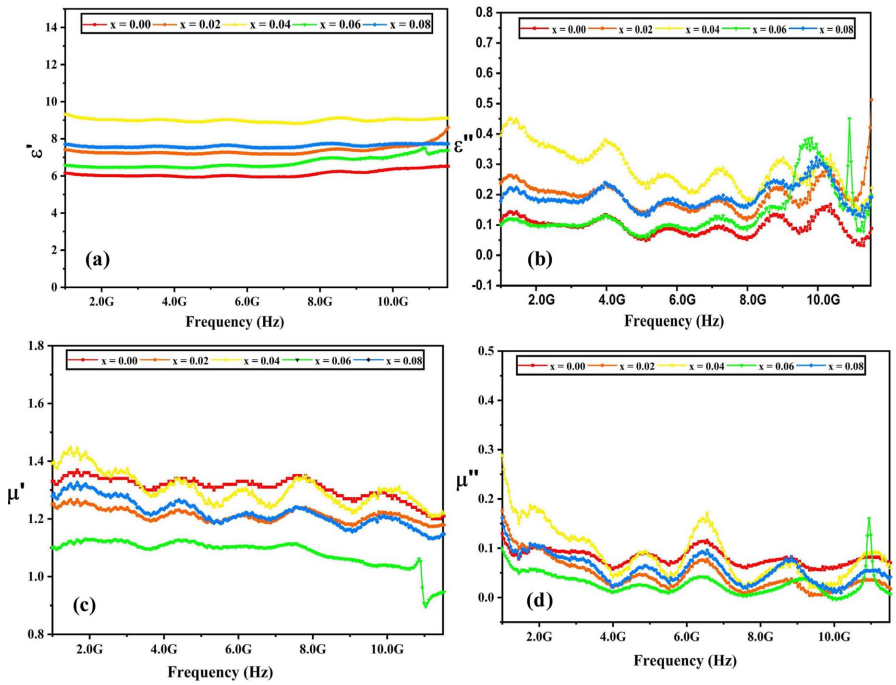

Figure 9. Frequency response of (a), (b): ε' and ε'' of complex permittivity (c), (d): μ' and μ'' of complex permeability for $BaFe_{12-x}Al_xO_{19}$, where $x = 0.00$, 0.02, 0.04, 0.06 and 0.08.

b) Dielectric and Magnetic Loss Tangents

The energy dissipation in the ferrite materials under electric and magnetic fields is indicated by the dielectric loss angle tangent ($\tan\delta_\varepsilon = \varepsilon''/\varepsilon'$) and magnetic loss angle tangent ($\tan\delta_\mu = \mu''/\mu'$). Wave absorption is more advantageous when the $\tan\delta$ value is higher [57]. **Figure 10** shows the frequency-dependent behavior of dielectric and magnetic loss tangent ($\tan\delta_\varepsilon$ and $\tan\delta_\mu$) for pure and Al-doped BHF over the frequency range of 1 - 12 GHz. $\tan\delta_\varepsilon$ and $\tan\delta_\mu$ behave similarly to the imaginary part of complex permittivity and permeability. $\tan\delta_\varepsilon$ falls between 0.01 and 0.06 over the entire frequency range and dopant concentrations. The dopant concentrations $x = 0.04$ and $x = 0.06$ have maximum and minimum values of 0.06

and 0.01, respectively. Pure BHF exhibits the lowest tangent dielectric loss at the highest frequency of 12 GHz. Similarly, $\tan\delta_\mu$ also remains close to zero in the near range of 0.08 - 0.18. The maximum value is observed for the composition of 0.04, and the minimum is for the composition of 0.06, respectively.

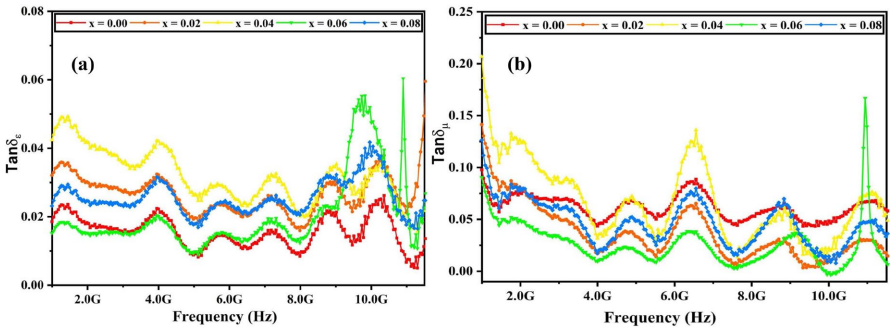

Figure 10. Frequency response of (a) $\tan\delta_\varepsilon$ and (b) $\tan\delta_\mu$ of pure and Al-doped BHF.

c) Cole-Cole Graphs

Figure 11 gives the pictorial representation of the Cole-Cole semicircular graphs for Al-doped BHF. **Figure 11(a)**, **Figure 11(b)** represents the ε'' vs ε' for $x = 0.00$, μ'' vs μ' for $x = 0.00$; (c), (d) ε'' vs ε' for $x = 0.02$, μ'' vs μ' for $x = 0.02$; (e), (f) ε'' vs ε' for $x = 0.06$, μ'' vs μ' for $x = 0.06$ Al ions composition. Debye relaxation is frequently revealed by plotting (Cole-Cole plot). These arcs point to different dielectric relaxation mechanisms, most likely interfacial polarisation at the borders of the MNP [58]. The Debye model is utilized to investigate polarization effects.

$$\varepsilon' = \varepsilon_\infty + \frac{\varepsilon_s - \varepsilon_\infty}{1+\omega^2\tau^2} \tag{6}$$

$$\varepsilon'' = \frac{(\varepsilon_s - \varepsilon_\infty)\omega\tau}{1+\omega^2\tau^2} \tag{7}$$

$$\left(\varepsilon' - \frac{\varepsilon_s + \varepsilon_\infty}{2}\right)^2 + (\varepsilon'')^2 = \left(\frac{\varepsilon_s - \varepsilon_\infty}{2}\right)^2 \tag{8}$$

where, ω is the angular frequency, τ is the relaxation period, ε_s is static permittivity, and ε_∞ is high-frequency permittivity. Cole-Cole plots for undoped and $x = 0.06$ samples have multiple arcs attributed to various dielectric relaxation processes, likely interfacial polarization from the buildup of charge carriers when the material is exposed to an alternating electric field at the heterogeneous interfaces between various microstructural areas such as grains, grain borders, and defect sites (low calcination) [59] [60]. At low GHz, conduction loss emerges in both samples, showing a tail indicating higher conductivity tiny Al addition ($x \approx 0.02$) for the $x = 0.02$ sample seems to simplify the relaxation spectrum (around a single semicircle), either by anchoring specific defect states so that one relaxation predominates or by lowering inhomogeneity. Like the Cole-Cole semicircle of ε'' vs ε' in dielectric absorbing materials, μ'' vs μ' curve also has a similar

Cole-Cole semicircle. Each similar Cole-Cole semicircle corresponds to a loss of resonance. The μ' vs μ' curves in Equation (4) are depicted based on Xing's research to validate the explanation of μ' and μ^{l} based on the natural resonance process [61].

$$\left(\mu''\right)^2+\left(\mu'\right)^2=\left(\frac{B_m}{\mu_o H_m}\right)^2 \tag{9}$$

where, B_m is maximum induction, and H_m is the maximum field. **Figure 11(b)**, **Figure 11(d)**, and f demonstrate that μ'' vs. μ' frequently deviates from a perfect semicircle because of magnetisation damping [40]. Resonance and *EC* are the primary causes of magnetic loss in the 2 - 18 GHz range. Losses from *EC*s are represented via Equation (16) as:

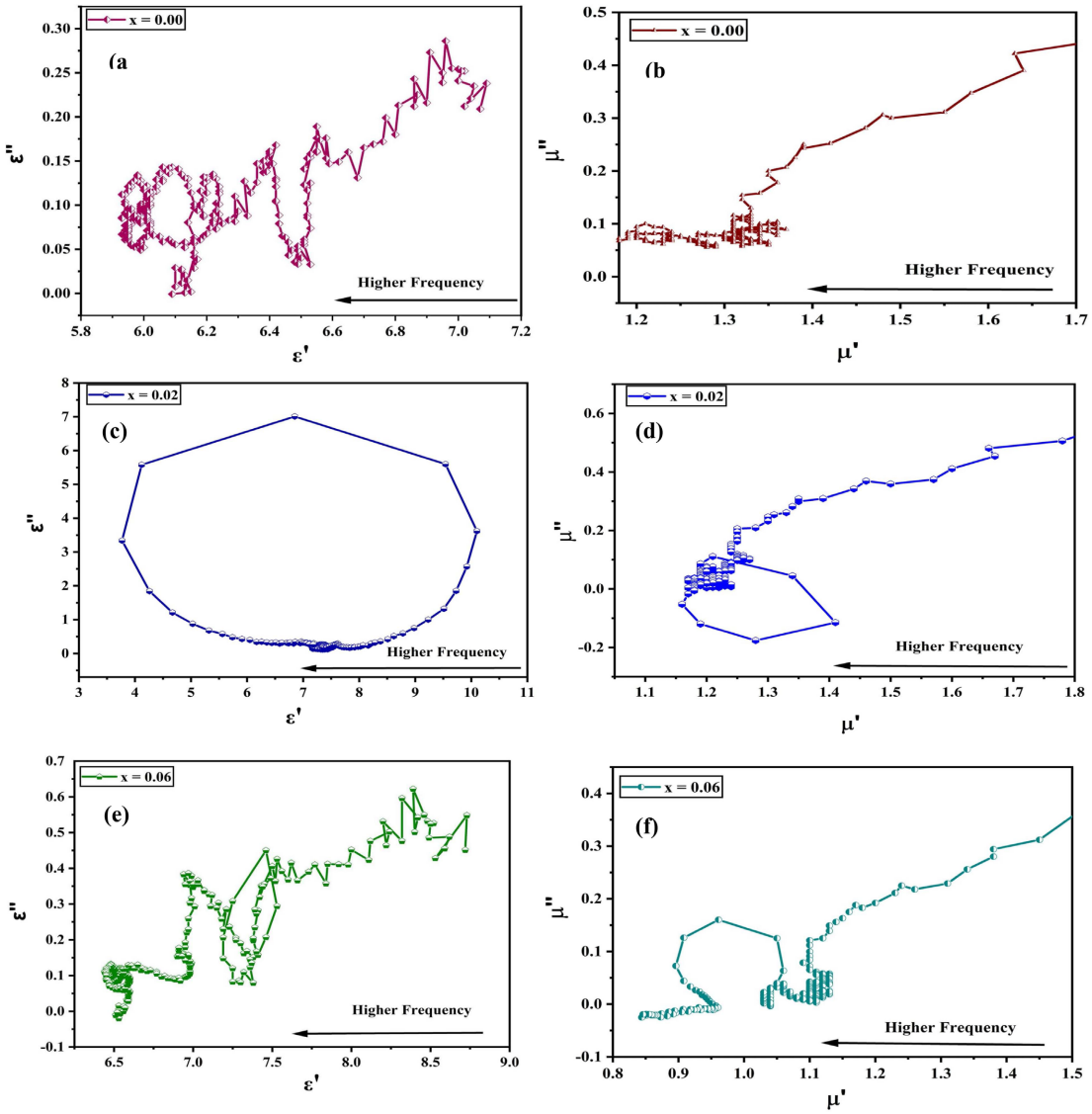

Figure 11. Cole-Cole graphs of $BaFe_{12-x}Al_xO_{19}$ (a) ε'' vs ε' for $x = 0.00$; (b) μ'' vs μ' for $x = 0.00$; (c) ε'' vs ε' for $x = 0.02$; (d) μ'' vs μ' for $x = 0.02$; (e) ε'' vs ε' for $x = 0.06$; (f) μ'' vs μ' for $x = 0.06$.

$$C_0 = \mu''\left(\mu'\right)^{-2} f^{-1} = 2\Pi\sigma d^2\mu_0 \tag{10}$$

In this equation, "*d*" stands for material thickness, μ_0 for free space permeability, and σ for electrical conductivity. The above equation suggests that the only cause of magnetic loss is EC loss, and that C_0 should be constant over the given frequency range. If the observed magnetic loss is solely due to EC loss, then the value of C_0 should not change as frequency rises. In this study, not all specimens meet the aforementioned criteria since the value of C_0 changes with frequency within the specified frequency range of 1 - 12 GHz (see **Figure 12**). Thus, resonance governs magnetic loss. Natural and exchange are the two major resonance losses in magnetic materials [61]. Natural resonance occurs if the material's characteristic frequency meets the incoming EM wave's cutoff, giving absorption [62].

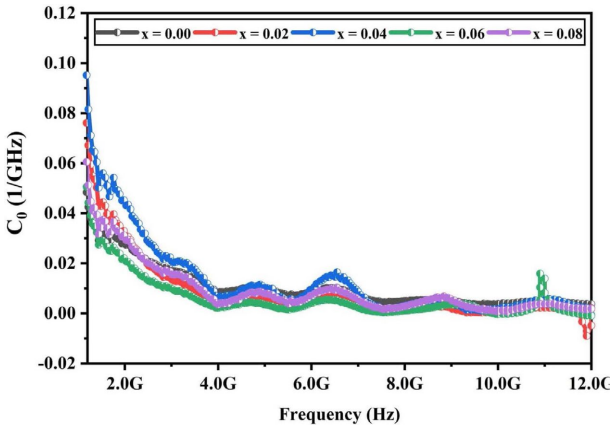

Figure 12. EC loss C_0 (1/GHz) for Ba $Al_xFe_{12-x}O_{19}$ for x = 0.00 - 0.08.

d) Microwave (mW) absorption properties

Standard measuring techniques, such as direct evaluation of air-space reflection (S_{11}) or indirect evaluation of EM characteristics, are used to categorise absorbing materials. One of the most important needs for absorbers is to reduce mirror reflection while matching the impedance of the air at the absorption contact [63]. Additionally, the material must show notable insulating and magnetic losses in order to enhance EM wave absorption. Additionally, it is anticipated that these materials would be used across a broad frequency range. It is recommended that the absorbent materials be thin and light [64].

The MW absorption properties of a sample are represented by the RL. According to transmission line theory, the RL values have been calculated using the complex ε and μ at a certain thickness d and frequency *f*. The value of reflection loss can be calculated using Equations (13) and (14) given below [65].

$$\mathrm{RL}\left(\mathrm{dB}\right) = -20\log\left|\frac{Z_{in} - Z_0}{Z_{in} + Z_0}\right| \tag{11}$$

$$z = \frac{Z_{in}}{Z_0} = \sqrt{\frac{\mu_r}{\varepsilon_r}}\tanh\left[j\frac{2\Pi fd}{c}\sqrt{\mu_r\varepsilon_r}\right] \tag{12}$$

where Z_0 represents the free space impedance (Ip), Z_{in} is the input Ip of the absorber, f gives frequency, d stands for thickness, μ_r and ε_r are the relative permeability and permittivity, and c is the speed of light in vacuum.

Figures 13(a)-(e) shows the MW absorption properties for Al-doped BHF, with varying frequency of 1 - 12 GHz. The MW absorption of EMWs at RL < −10 dB is thought suitable as it can vanish above 90% of the input EMW. For practical application, MW absorbers mostly aim for the EM absorption at RL < −20 dB, meaning that above 99% of the entering EMW is absorbed. The reflection loss performance is investigated by showing RL diagrams of two-dimensional Al-doped BHF nano-particles Ba $Al_xFe_{12-x}O_{19}$ at various thicknesses for composition x = 0.00, 0.02, 0.04, 0.06, and 0.08, respectively. The addition of a dopant has a significant impact on RL values, because it drops to a lower value of RL. As the frequency rises, the thickness range of the material expands.

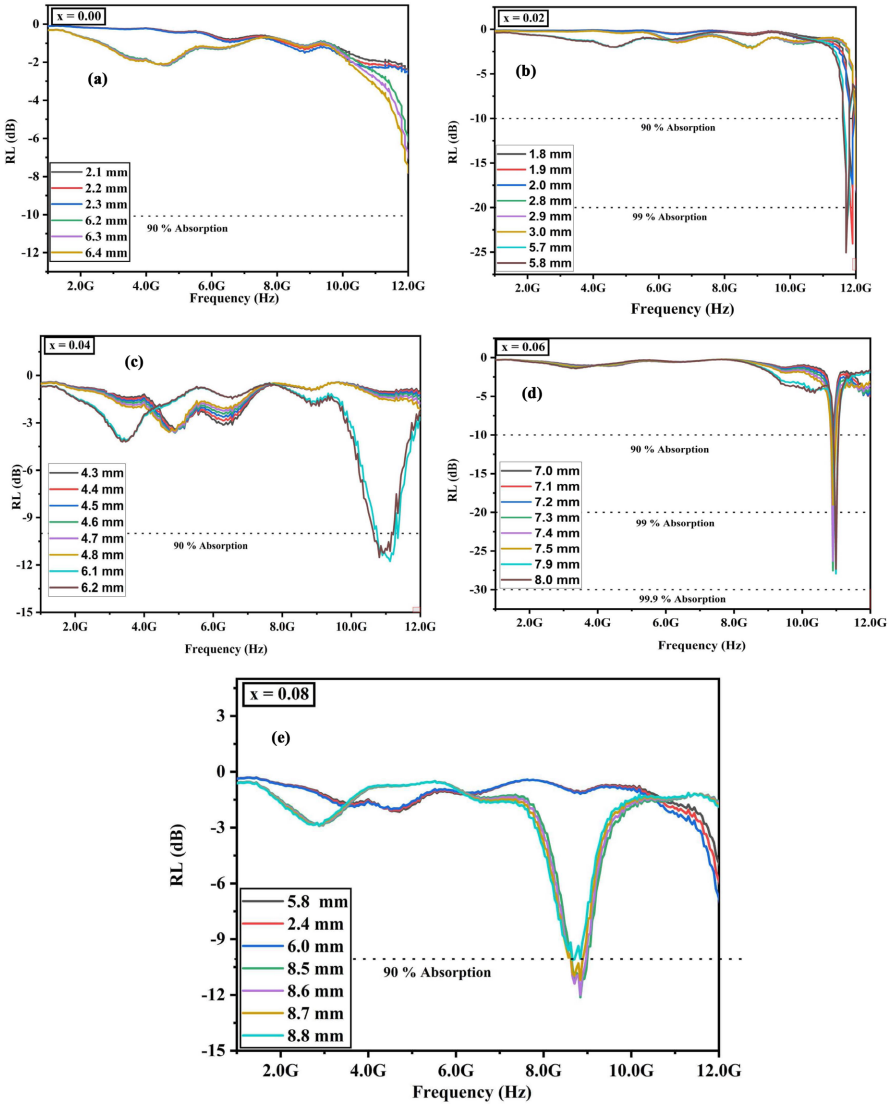

Figure 13. RL value of Ba $Al_xFe_{12-x}O_{19}$ at various thicknesses for (a): x = 0.00 (b): for x = 0.02 (c) for x = 0.04 (d) for x = 0.06 (e) for x = 0.08.

For pure BHF, *i.e.*, $x = 0.00$, there is no reflection loss observed in the frequency range of 1 - 12 GHz. For $x = 0.02$, the reflection loss value significantly declines to $RL_{min} = -25.05$ dB, for $d_m = 5.8$ mm at 11.7 GHz. The range of $EBW_{RL<-10dB} = 0.3$ increases with an increase in dopant amount. However, $x = 0.02$ also gives the effective values of $RL_{min} < -20$ dB for lower thickness. For $d_m = 1.9$ mm, $RL_{min} = -24.00$ dB, at the frequency of 11.9 GHz. The $EBW_{RL<-10dB}$ for the same thickness is 0.2 GHz. It is evident from the data that the dopant concentration has a greater effect on the thickness at which the material exhibits the reduced reflection loss. The dopant concentration $x = 0.02$ could be considered as satisfactory, because it provides a drop in both the material's thickness range and in reflection loss.

As the dopant concentration increases, *i.e.*, for $x = 0.04$, $RL_{min} = -11.51$ dB and -11.76 dB, for $d_m = 6.2$ mm and 6.1 mm at 10.81 GHz and 11.1 GHz, respectively. The range of $EBW_{RL<-10dB} = 0.58$ and 0.67 GHz. This dopant amount has increased the value of the effective bandwidth by 0.3 GHz.

Further increase in the dopant amount would increase the matching thickness as shown in **Figure 13(d)**, **Figure 13(e)**. For $x = 0.06$, $RL_{min} = -27.55$ dB and -27.93 dB, for $d_m = 7.3$ mm and 7.9 mm at 10.9 GHz and 10.99 GHz, respectively. The range of $EBW_{RL<-10dB} = 0.1$ and 0.8 GHz, respectively. The value of RL_{min} decreases with further increase in dopant concentration, *i.e.*, the lowest value of -12.00 dB is observed for composition $x = 0.08$ at the thickness of 8.6 mm.

e) Further discussion

Efficient MW attenuation must be considered to achieve highly effective MW absorption. The efficiency with which an absorber attenuates EM waves is demonstrated by the value of the attenuation constant (α). The value α increases with the strength of the EM attenuation ability [66] [67]. **Figure 14** displays the α curves of pure and Al-doped BHF NPs.

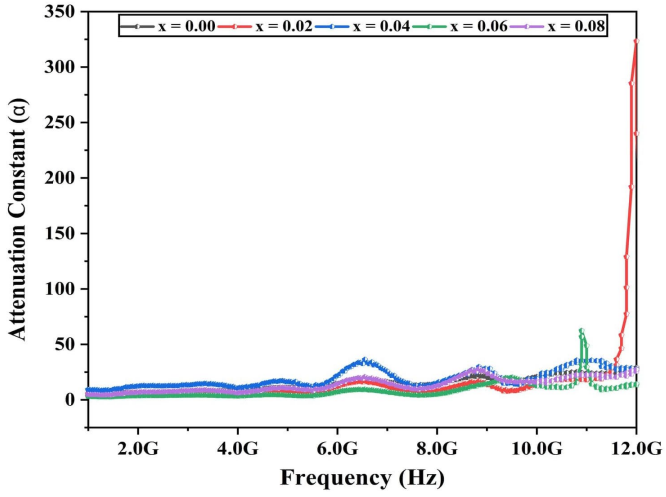

Figure 14. Attenuation constant for $BaAl_xFe_{12-x}O_{19}$, for $x = 0.00$ - 0.08.

For every dopant concentration, or $x = 0.00$ - 0.08, the value of α falls between 2 and 60. With a change in dopant concentration, α varies marginally up to 10

GHz, but beyond that, the fluctuation in α becomes more noticeable. Even while the sample with composition $x = 0.02$ exhibits resonance at 12 GHz, it attains the maximum value of 323.42. The sample at dopant concentrations $x = 0.04$ shows the maximum value of α.

The substitution of Al into BHF NP effectively modifies the EM parameters and significantly enhances the MW absorption characteristics. The composition $x = 0.02$ achieved a decline in RL_{min} with reduced thickness.

4. Conclusion

In summary, we investigated the structural, morphological, FTIR, magnetic, and microwave absorption behavior of $BaFe_{12-x}Al_xO_{19}$ ($x = 0.00$, 0.02, 0.04, 0.06, and 0.08) hexaferrites. Our investigation uncovers that structural and other related functional properties are strongly governed by the nonmagnetic Al^{3+} doping. All compounds crystallize in the M-type hexagonal phase, where lattice parameters systematically contract with Al^{3+} doping. A nonuniform distribution, along with hexagon morphology, of particles was observed in morphological analysis. FTIR analysis verified the hexagonal crystalline phase, evidenced by metal-oxygen stretching and bending vibrations. Hard ferromagnetic nature and a large coercive field value, which further increased (up to ~59%) with the dopant, were demonstrated in the magnetic results. Microwave absorption results have shown synergistic effects in dielectric/magnetic losses and strong electromagnetic attenuation. This enables efficient microwave absorption/reflection loss, a wide effective absorption bandwidth, and a thin matching thickness in such systems. These findings highlight the promising role of Al^{3+} doping in hexaferrite materials for advancing communication systems and tourism, further encouraging research and development in this area.

Acknowledgements

With project number ANRF/PAIR/2025/000006/PAIR-A(G), the authors would like to sincerely thank the Anusandhan National Research Foundation (ANRF) for supporting us under the Partnerships for Accelerated Innovation and Research (PAIR) programme.

Conflicts of Interest

The authors declare no conflicts of interest regarding the publication of this paper.

References

[1] Mahanta, A., Samal, R. and Sahu, N.C. (2026) Harnessing Renewable Energy to Advance Sustainable Tourism and Green Growth: A G20 Countries' Perspective. *Energy Research Letters*, **7**, 1-6. https://doi.org/10.46557/001c.156401

[2] Rasool, H., Maqbool, S. and Tarique, M. (2021) The Relationship between Tourism and Economic Growth among BRICS Countries: A Panel Cointegration Analysis. *Future Business Journal*, **7**, Article No. 1. https://doi.org/10.1186/s43093-020-00048-3

[3] You, W., Zhang, Y. and Lee, C. (2021) Climate Risk, Economic Stability, and Tourism: A Cross-Sectionally Dependent Heterogeneous Panel Causality Analysis. *Energy Research Letters*, **2**, 1-5. https://doi.org/10.46557/001c.25723

[4] Rangarajan, S.S., Shiva, C.K., Collins, E.R. and Senjyu, T. (2025) Electric Vehicle Motors Free of Rare-Earth Elements—An Overview. *Machines*, **13**, Article 702. https://doi.org/10.3390/machines13080702

[5] Mohammed, I., Mohammed, J. and Srivastava, A.K. (2022) Recent Progress in Hexagonal Ferrites Based Composites for Microwave Absorption. *Crystal Research and Technology*, **58**, Article ID: 2200200. https://doi.org/10.1002/crat.202200200

[6] Riba, J., López-Torres, C., Romeral, L. and Garcia, A. (2016) Rare-Earth-Free Propulsion Motors for Electric Vehicles: A Technology Review. *Renewable and Sustainable Energy Reviews*, **57**, 367-379. https://doi.org/10.1016/j.rser.2015.12.121

[7] Dippong, T. (2021) Characterization and Applications of Metal Ferrite Nanocomposites. *Nanomaterials*, **12**, Article 107. https://doi.org/10.3390/nano12010107

[8] Vidya, Y.S., Manjunatha, H.C., Sridhar, K.N., Seenappa, L., Munirathnam, R. and Chinnappareddy, B. (2023) Brief Review on Magnetic Properties of Nanoferrites. *Inorganic Chemistry Communications*, **158**, Article ID: 111408. https://doi.org/10.1016/j.inoche.2023.111408

[9] Majeed, A., Khan, M.A., Ahmad, A., Javed, Z., Lodhi, M.Y., Khan, S., *et al.* (2025) Promising X-Type Hexagonal Ferrites for High Frequency Applications; Synthesis and Characterizations. *Ceramics International*, **51**, 32305-32317. https://doi.org/10.1016/j.ceramint.2025.04.417

[10] Gorbachev, E.A., Trusov, L.A., Sleptsova, A.E., Kozlyakova, E.S., Alyabyeva, L.N., Yegiyan, S.R., *et al.* (2020) Hexaferrite Materials Displaying Ultra-High Coercivity and Sub-Terahertz Ferromagnetic Resonance Frequencies. *Materials Today*, **32**, 13-18. https://doi.org/10.1016/j.mattod.2019.05.020

[11] Irfan, M., Shamshad, I., Ashiq, A.R., Shabbir, H.G., Idrees, T., Khan, F., *et al.* (2025) A Critical Review on Structural, Magnetic, and Electrical Properties of R-Type Hexaferrites for Microwave Applications. *Next Materials*, **9**, Article ID: 101204. https://doi.org/10.1016/j.nxmate.2025.101204

[12] Dehghani Dastjerdi, O., Shokrollahi, H. and Mirshekari, S. (2023) A Review of Synthesis, Characterization, and Magnetic Properties of Soft Spinel Ferrites. *Inorganic Chemistry Communications*, **153**, Article ID: 110797. https://doi.org/10.1016/j.inoche.2023.110797

[13] Chang, T. (2020) Ferrite Materials and Applications. In: Han, M.G., Ed., *Electromagnetic Materials and Devices*, IntechOpen, 137-349. https://doi.org/10.5772/intechopen.84623

[14] Sharma, D., Rohit, Singh, V., Dogra, A. and Singh, M. (2024) Aluminium and Praseodymium Doped M-Type Hexaferrites for Electric Vehicle Applications. *Ceramics International*, **50**, 24815-24822. https://doi.org/10.1016/j.ceramint.2024.04.217

[15] Duglet, R., Chauhan, A., Sharma, D., Thakur, A. and Singh, M. (2024) Investigation on Microwave Absorption Properties of Bismuth Ions Doped Barium Hexaferrites. *Journal of Materials Science: Materials in Electronics*, **35**, Article No. 654. https://doi.org/10.1007/s10854-024-12418-6

[16] Chandel, M., Pratap Singh, V., Jasrotia, R., Singha, K. and Kumar, R. (2020) A Review on Structural, Electrical and Magnetic Properties of Y-Type Hexaferrites Synthesized by Different Techniques for Antenna Applications and Microwave Absorb-

ing Characteristic Materials. *AIMS Materials Science*, **7**, 244-268. https://doi.org/10.3934/matersci.2020.3.244

[17] Pullar, R.C. (2012) Hexagonal Ferrites: A Review of the Synthesis, Properties and Applications of Hexaferrite Ceramics. *Progress in Materials Science*, **57**, 1191-1334.

[18] Shepherd, P., Mallick, K.K. and Green, R.J. (2007) Magnetic and Structural Properties of M-Type Barium Hexaferrite Prepared by Co-Precipitation. *Journal of Magnetism and Magnetic Materials*, **311**, 683-692. https://doi.org/10.1016/j.jmmm.2006.08.046

[19] Kaur, H., Bhatia, K.S., Tewari, B.S., Mandal, P. and Dhyani, A. (2022) Influence of Co-In Doping in M-Type Barium-Strontium Hexagonal Ferrite on Microwave Absorption. *Journal of Electronic Materials*, **51**, 4152-4160. https://doi.org/10.1007/s11664-022-09731-3

[20] Liao, W., Huang, K., Xu, W., Yu, J., Li, P. and Xu, J. (2024) Broadband Microwave Absorption and Electromagnetic Properties of Gd-Al-Co-Doped M-Type Barium Hexaferrite in 2-18 GHz Range. *Journal of Magnetism and Magnetic Materials*, **612**, Article ID: 172609. https://doi.org/10.1016/j.jmmm.2024.172609

[21] Naqvi, S.T.A., Godara, S.K., Ray, B., Datar, S. and Singh, C. (2025) Tunable Structural, Magnetic, Complex Permittivity/Permeability, and Reflection Loss Parameters of Co^{2+} and Ni^{2+}-Co-Doped M-Type Strontium Ferrites for Microwave Absorber Applications. *Journal of Materials Science: Materials in Electronics*, **36**, Article No. 213. https://doi.org/10.1007/s10854-025-14252-w

[22] Abbas, W., Ahmad, I., Kanwal, M., Murtaza, G., Ali, I., Azhar Khan, M., *et al.* (2015) Structural and Magnetic Behavior of Pr-Substituted M-Type Hexagonal Ferrites Synthesized by Sol-Gel Autocombustion for a Variety of Applications. *Journal of Magnetism and Magnetic Materials*, **374**, 187-191. https://doi.org/10.1016/j.jmmm.2014.08.029

[23] Mahmoud, M.H., Hassan, A.M., Said, A.E.A. and Taha, T.A. (2022) Structural, Magnetic, and Catalytic Studies of Microwave-Combustion/Ball-Mill Synthesized Zinc Ferrite Nanoparticles. *Inorganic Chemistry Communications*, **144**, Article ID: 109932. https://doi.org/10.1016/j.inoche.2022.109932

[24] Yasin, S.M. (2023) Superparamagnetic $Ni_{0.5}Zn_{0.5}Fe_2O_4$ Nanoparticles Prepared by Ball-Milling. *Applied Physics A*, **129**, Article No. 672. https://doi.org/10.1007/s00339-023-06954-x

[25] Piotto, V., *et al.* (2022) Synthesis of Magnetic Nanoparticles by Laser Ablation of Strontium Ferrite under Water and Their Characterization by Optically Detected Magnetophoresis Supported by BEM Calculations. *Journal of Materials Chemistry C*, **10**, 3819-3825.

[26] Saremi, A., Mirkazemi, S.M., Sazvar, A. and Rezaie, H. (2024) Controlling Magnetic and Surface Properties of Cobalt Ferrite Nanoparticles: A Comparison of Co-Precipitation and Solvothermal Synthesis Methods. *Solid State Sciences*, **148**, Article ID: 107432. https://doi.org/10.1016/j.solidstatesciences.2023.107432

[27] Moatoshi, Sah, S.K., Kaushik, S.D. and Borah, J.P. (2024) Structural and Magnetic Properties of M-Type Hexaferrite Nanoparticles: A Comparative Analysis of $BaFe_{12}O_{19}$ and $SrFe_{12}O_{19}$ Synthesized via Chemical Co-Precipitation. *Ceramics International*, **50**, 22599-22607. https://doi.org/10.1016/j.ceramint.2024.03.361

[28] Wang, X., Wang, B., Wei, S., Wang, Y. and Liang, Y. (2023) Effect of Sintering Temperature on the Microstructure, Magnetic, and Microwave Absorption Properties of M-Type Barium Ferrite Nanoparticles Prepared by Sol-Gel Method. *Journal of Materials Science: Materials in Electronics*, **34**, Article No. 1045. https://doi.org/10.1007/s10854-023-10400-2

[29] Borhan, A.I., Iordan, A.R., Ghercă, D. and Palamaru, M.N. (2023) Ferrite Nanoparticles by Sol-Gel Method. In: Singh, J.P., Chae, K.H., Srivastava, R.C. and Caltun, O.F., Eds., *Ferrite Nanostructured Magnetic Materials*, Elsevier, 103-119. https://doi.org/10.1016/b978-0-12-823717-5.00047-4

[30] Sharma, I., Vineet Sharma, M. and Sharma, P. (2022) A Review on Synthesis and Characterization of MnZn Ferrite Nanoparticles via Citrate Precursor Method. *Peer Reviewed and Refereed Journal*, **11**, 57-67.

[31] Sharma, D., Duglet, R., Singh, V., Mohd, Y., Dogra, A. and Singh, M. (2026) Tailoring Magnetic Parameters of M-Type Hexaferrites via Nd-Al Doping for Rare Earth Free Permanent Magnet in Ev's. *Physics Letters A*, **579**, Article ID: 131517. https://doi.org/10.1016/j.physleta.2026.131517

[32] Pandav, R.S., Pujari, S.S., Bagade, A.A., Gurme, V.M. and Sankpal, U.B. (2026) Structural, Magnetic, and Dielectric Properties of Cr Substituted Cobalt Ferrite Nanoparticles Synthesized by Citrate-Gel Auto-Combustion. *Journal of Materials Science: Materials in Electronics*, **37**, Article No. 458. https://doi.org/10.1007/s10854-026-16888-8

[33] Liaquat, A., Anis-ur-Rehman, M. and ul Haq, A. (2020) Impact of Gd Doping on the Dielectric and Magnetic Properties of (Sr-ba) Fe12o19 Nanoparticles. *Journal of Alloys and Compounds*, **822**, Article ID: 153561. https://doi.org/10.1016/j.jallcom.2019.153561

[34] Gulbadan, S., Khan, M.A., Rasool, R.T., Zelai, T., Mahmood, K., Shahid, M., *et al.* (2023) Investigation of Crystal Structure, Photoluminescence, and Raman Studies of Sm-Co Substituted Ba-Sr M-Type Hexaferrites. *Ceramics International*, **49**, 18076-18083. https://doi.org/10.1016/j.ceramint.2023.02.176

[35] Mohammed, J., Suleiman, A.B., Hafeez, H.Y., Carol T, T.T., Sharma, J., Bhadu, G.R., *et al.* (2018) Effect of Heat-Treatment on the Magnetic and Optical Properties of $Sr_{0.7}Al_{0.3}Fe_{11.4}Mn_{0.6}O_{19}$. *Materials Research Express*, **5**, Article ID: 086106. https://doi.org/10.1088/2053-1591/aad1e5

[36] Godara, S.K., Kaur, M.P., Kaur, V., Malhi, P.S., Singh, M., Verma, S., *et al.* (2022) Investigation of Microstructural and Magnetic Properties of Ca^{2+} Doped Strontium Hexaferrite Nanoparticles. *Journal of King Saud University—Science*, **34**, Article ID: 101963. https://doi.org/10.1016/j.jksus.2022.101963

[37] Carol, T.T.T., *et al.* (2025) Crystal Structure Refinement, Bond Length, Raman Spectroscopy and Magnetic Properties of Al^{3+}- and Ce^{3+}-Codoped M-Type Barium Hexagonal Ferrite. *Inorganic Chemistry Communications*, **173**, Article ID: 113771.

[38] Luo, H., Rai, B.K., Mishra, S.R., Nguyen, V.V. and Liu, J.P. (2012) Physical and Magnetic Properties of Highly Aluminum Doped Strontium Ferrite Nanoparticles Prepared by Auto-Combustion Route. *Journal of Magnetism and Magnetic Materials*, **324**, 2602-2608. https://doi.org/10.1016/j.jmmm.2012.02.106

[39] Cullity, B.D. (1978) Elements of X-Ray Diffraction. Addison-Wesley Publishing Company.

[40] Xu, W., Liao, W., Zhou, H., Wang, L., Huang, K., Li, P., *et al.* (2024) M-Type Ba-Hexaferrite Nanoplates with Exceptional Microwave Absorption Properties. *ACS Applied Electronic Materials*, **6**, 2759-2766. https://doi.org/10.1021/acsaelm.4c00307

[41] Verma, R., Chauhan, A., Batoo, K.M., Kumar, R., Hadi, M. and Raslan, E.H. (2021) Structural, Morphological, and Optical Properties of Strontium Doped Lead-Free BCZT Ceramics. *Ceramics International*, **47**, 15442-15457. https://doi.org/10.1016/j.ceramint.2021.02.110

[42] Gilani, Z.A., Ul Islam, S., Khan Asghar, H.M.N.U.H., Hussain, R. and Ahmad Shaikh,

F. (2021) Impact of Lanthanum Doping on the Structural, Electrical, and Magnetic Properties of $BaFe_{12}O_{19}$ Nano Particles. *Journal of Materials and Physical Sciences*, **2**, 22-32. https://doi.org/10.52131/jmps.2021.0201.0013

[43] Naqvi, S.T.A., Godara, S.K., Ray, B., Datar, S. and Singh, C. (2025) Investigation of Structural, Hysteresis, and Microwave Dielectric/Magnetic Properties of Co-Zn Doped M-Type Strontium Hexaferrites for Light-Weight Microwave Absorber Applications. *Emergent Materials*, **8**, 3331-3353. https://doi.org/10.1007/s42247-025-01034-7

[44] Sertkol, M., Köseoğlu, Y., Baykal, A., Kavas, H., Bozkurt, A. and Toprak, M.S. (2009) Microwave Synthesis and Characterization of Zn-Doped Nickel Ferrite Nanoparticles. *Journal of Alloys and Compounds*, **486**, 325-329. https://doi.org/10.1016/j.jallcom.2009.06.128

[45] Atkare, S.S., Shirsath, S.E., Batoo, K.M., Ijaz, M.F., Deshmukh, V.J., Kadam, R.H., *et al.* (2025) Enhancing the Magnetic and Dielectric Properties of M Type Strontium Hexaferrite Nanoparticles via Aluminum Substitution: A Sol-Gel Synthesis Approach. *Journal of Sol-Gel Science and Technology*, **116**, 421-433. https://doi.org/10.1007/s10971-025-06712-w

[46] Rana, K., Thakur, P., Tomar, M., Gupta, V. and Thakur, A. (2018) Investigation of Cobalt Substituted M-Type Barium Ferrite Synthesized via Co-Precipitation Method for Radar Absorbing Material in Ku-Band (12-18GHz). *Ceramics International*, **44**, 6370-6375. https://doi.org/10.1016/j.ceramint.2018.01.028

[47] Anjum, S., Hameed, S., Awan, M.S., Amed, E. and Sattar, A. (2017) Effect of Strontium Doped M-Type Bariam Hexa-Ferrites on Structural, Magnetic and Optical Properties. *Optik*, **131**, 977-985. https://doi.org/10.1016/j.ijleo.2016.11.205

[48] Ijaz, M., Ullah, H., Ali Al-Asbahi, B., Ullah Khan, M., Abbas, Z. and Ullah Asif, S. (2024) Co-Precipitation Method Followed by Ultrafast Sonochemical Synthesis of Aluminium Doped M Type $BaFe_{11.4-X}Al_xCo_{0.6}O_{19}$ Hexaferrites for Various Applications. *Journal of Magnetism and Magnetic Materials*, **589**, Article ID: 171559. https://doi.org/10.1016/j.jmmm.2023.171559

[49] Maltoni, P., Dokala, R.K., Pramanik, P., Araujo, R., Edvinsson, T., Ivanov, S.A., *et al.* (2026) Temperature Dependent Magnetic and Structural Properties of Al Substituted Nanostructured Hexaferrites with Large Coercive Fields. *Acta Materialia*, **313**, Article ID: 122273. https://doi.org/10.1016/j.actamat.2026.122273

[50] Albanese, G., Carbucicchio, M. and Deriu, A. (1974) Temperature Dependence of the Sublattice Magnetizations in Al- and Ga-Substituted M-Type Hexagonal Ferrites. *Physica Status Solidi* (*a*), **23**, 351-358. https://doi.org/10.1002/pssa.2210230202

[51] Kumar, S., Supriya, S., Pradhan, L.K., Pandey, R. and Kar, M. (2018) Simultaneous Effect of Crystal Lattice and Non Magnetic Substitution on Magnetic Properties of Barium Hexaferrite. *AIP Conference Proceedings*, **1953**, 1-4. https://doi.org/10.1063/1.5033105

[52] Kittel, C. (1957) Introduction to Solid State Physics. Wiley.

[53] Atkare, S.S., Alone, S.T., Fulari, A.V., Dhage, V.N., Kadam, R.H., Shirsath, S.E., *et al.* (2025) Design of Multifunctional Rare Earth Dy-Ce Substituted $BaFe_{12}O_{19}$ Nanoparticles for X-Band Microwave Absorption and EMI Shielding. *Inorganic Chemistry Communications*, **179**, Article ID: 114805. https://doi.org/10.1016/j.inoche.2025.114805

[54] Micheli, D. (2012) Radar Absorbing Materials and Microwave Shielding Structures Design. LAP Lambert Academic Publishing.

[55] Li, M., Cao, X., Zheng, S. and Qi, S. (2017) Ternary Composites RgO/MoS_2@Fe_3O_4:

Synthesis and Enhanced Electromagnetic Wave Absorbing Performance. *Journal of Materials Science*: *Materials in Electronics*, **28**, 16802-16812. https://doi.org/10.1007/s10854-017-7595-x

[56] Wang, C., Hu, S., Han, X., Huang, W. and Tian, L. (2013) Controlled Synthesis and Microwave Absorption Property of Chain-Like Co Flower. *PLOS ONE*, **8**, e55928. https://doi.org/10.1371/journal.pone.0055928

[57] Wang, G., Ma, Z., Zheng, Y., Cheng, L., Xing, H. and Li, Z. (2024) Effect of Rare-Earth Ytterbium Doping on the Microwave Absorption Performance of Nickel-Cobalt Ferrite. *RSC Advances*, **14**, 38345-38352. https://doi.org/10.1039/d4ra06136e

[58] Singh, V., Rohit, Deepika, Batoo, K.M. and Singh, M. (2025) Lithium-Zinc Ferrite-Based Chitosan/Graphene Oxide Nanocomposite: An Efficient Microwave Absorbing Material for C and X Bands. *Composites Communications*, **56**, Article ID: 102383. https://doi.org/10.1016/j.coco.2025.102383

[59] Bai, M., Zhao, D., Zhang, Q., Wang, B. and Zhang, Y. (2026) Advances in Structural Design and High-Temperature Resistance of Electromagnetic Absorbing Materials: A Comprehensive Review. *Composites Part A*: *Applied Science and Manufacturing*, **202**, Article ID: 109464. https://doi.org/10.1016/j.compositesa.2025.109464

[60] Zia, T.U.H., Gul, I.H., Kebaili, I., Alomayrah, N., Ara, B. and Gul, K. (2025) Cole-Cole Plot Analysis of Complex Permittivity for Investigating the Dielectric Relaxation Process in Polystyrene Based High-K Nanocomposite. *Materials Chemistry and Physics*, **343**, Article ID: 131048. https://doi.org/10.1016/j.matchemphys.2025.131048

[61] Bao, S., Zhang, M., Jiang, Z., Xie, Z. and Zheng, L. (2023) Advances in Microwave Absorbing Materials with Broad-Bandwidth Response. *Nano Research*, **16**, 11054-11083. https://doi.org/10.1007/s12274-023-5654-6

[62] Chen, W., Han, M. and Deng, L. (2010) High Frequency Microwave Absorbing Properties of Cobalt Nanowires with Transverse Magnetocrystalline Anisotropy. *Physica B: Condensed Matter*, **405**, 1484-1488. https://doi.org/10.1016/j.physb.2009.12.026

[63] Sani, Y., Azis, R.S., Ismail, I., Yaakob, Y. and Mohammed, J. (2023) Enhanced Electromagnetic Microwave Absorbing Performance of Carbon Nanostructures for Rams: A Review. *Applied Surface Science Advances*, **18**, Article ID: 100455. https://doi.org/10.1016/j.apsadv.2023.100455

[64] Elmahaishi, M.F., Azis, R.S., Ismail, I. and Muhammad, F.D. (2022) A Review on Electromagnetic Microwave Absorption Properties: Their Materials and Performance. *Journal of Materials Research and Technology*, **20**, 2188-2220. https://doi.org/10.1016/j.jmrt.2022.07.140

[65] Zuo, D., Jia, Y., Xu, J. and Fu, J. (2023) High-Performance Microwave Absorption Materials: Theory, Fabrication, and Functionalization. *Industrial & Engineering Chemistry Research*, **62**, 14791-14817. https://doi.org/10.1021/acs.iecr.3c02150

[66] Li, W., Li, C., Lin, L., Wang, Y. and Zhang, J. (2019) All-Dielectric Radar Absorbing Array Metamaterial Based on Silicon Carbide/Carbon Foam Material. *Journal of Alloys and Compounds*, **781**, 883-891. https://doi.org/10.1016/j.jallcom.2018.12.010

[67] Zhao, B., Zhao, W., Shao, G., Fan, B. and Zhang, R. (2015) Morphology-Control Synthesis of a Core-Shell Structured Nicu Alloy with Tunable Electromagnetic-Wave Absorption Capabilities. *ACS Applied Materials & Interfaces*, **7**, 12951-12960. https://doi.org/10.1021/acsami.5b02716